A Dual Mode, Thin and Wideband MIMO Antenna System for Seamless Integration on UAV

ZUBAIR AKHTER (Member, IEEE), **RANA M. BILAL**, AND **ATIF SHAMIM** (Senior Member, IEEE)

Electrical and Computer Engineering Department, CEMSE Division, King Abdullah University of Science and Technology, Thuwal 23955, Saudi Arabia

CORRESPONDING AUTHOR: Z. AKHTER (e-mail: zubair.akhter@kaust.edu.sa)

ABSTRACT Unmanned Aerial Vehicles (UAV's), also known as autonomous drones, are being utilized for a variety of applications such as disaster management, search and rescue, surveillance, and remote monitoring. The wireless link to transfer the data from the drone to the ground station or another drone is critical for such applications. Antenna, being the most important part of that wireless link, must be designed such that it seamlessly integrates with the drone without affecting its flight. This means the antenna must be thin, lightweight, conformal, and provide wide coverage. On the other hand, antenna's performance must not be deteriorated due to UAV mounting, so antennas with ground planes are preferred. Further, to cater for high data rate applications, a large bandwidth is required, which is difficult to achieve on thin substrates. In this paper, a dual band design is presented that addresses all the key requirements for a drone antenna. Specifically, the bandwidth is enhanced without increasing the substrate thickness. The proposed dual-mode antenna demonstrates one of the largest bandwidths (4% at 2.4 GHz and 7% at 5.2 GHz) on a thin substrate ($0.0128 \lambda_0$) and presents one of the highest gain ($\sim$10dBi) in comparison to the published UAV antennas. It is shown that the antenna's performance does not deteriorate for moderate bending conditions. Finally, a 3-element triangular multiple input multiple output (MIMO) configuration is designed and seamlessly integrated with the UAV body to demonstrate its efficacy.

INDEX TERMS Antenna, bandwidth improvement, circular microstrip patch, dual-mode, parasitic patches, UAVs.

I. INTRODUCTION

IN THE last decade, UAVs have received considerable attention from industries to provide services for a number of applications such as drones photography, mapping, surveillance, search and rescue, wild-life monitoring, precision agriculture, shipping, and delivery, etc. In a recent market survey, it is predicted that UAV's market will continue to grow at a compound rate of 15.37% and is expected to be $47.76 billion by 2025 [1]. Few of the above-mentioned applications such as surveillance, search, and rescue require real-time HD video transmission from air-borne drones to the ground stations. The transmission of HD video for longer distances can be achieved by employing antennas with larger bandwidths and higher gains. Further, the UAV antennas must be light-weight, thin and conformal so that they can be integrated with the UAV body in a seamless fashion.

The commonly used antennas for UAVs are blade antennas (mostly $\lambda/4$ monopole radiator), printed dipoles or monopoles, cavity-backed annular slot antennas, and microstrip patch [2]–[13]. The blade antenna requires an aerodynamic enclosure that adds more payload and can affect overall antenna gain [2]. Due to protruding nature of conventional wire monopoles, printed/conformal monopoles can provide a better alternative due to less weight and seamless/conformal integration with the subject [4], [6], [8], [14], [15]. Printed/conformal monopoles can provide a decent impedance bandwidths and can be also be designed for multiband operations however their characteristics, i.e., resonant frequency sometimes changes while mounted on a drones body. Therefore, the constitutive properties of drone's body material are required in advance for designing an efficient antenna. However, conformal monopole designs with full ground plane [4], [6] suffer
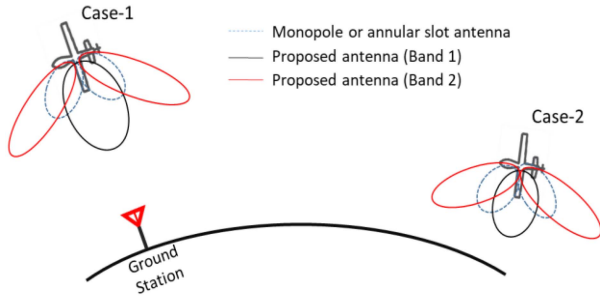
FIGURE 1. Radiation coverage for various scenarios for the proposed antenna and the conventional antennas.

FIGURE 2. Antenna model description: reference circular patch.

in terms of the realized bandwidths and higher thickness (typically 10-18 mm) that requires significant recess of drone's body material to have seamless integration. Removing more material from drone's body, e.g., wings or fuselage to fit such an antenna can make that part mechanically vulnerable and may require additional fiberglass lamination. Being a low profile among the all, an annular slot antenna seems more suitable for the seamless integration. However, thin annular slot antenna and printed/conformal monopoles have relatively low gains around 1.0-2.5 dBi [5], [6], [9]. Apart from low in gain, they have some coverage issues as mentioned in Fig. 1 due to the null in the broadside. For example, the coverage issues can be in the situations where drone is flying either directly on top (case 1) or far away from the ground station at a low altitude (case 2). In few papers, the antenna arrays have been embedded in the drone's body, e.g., wings [7], and its trunk [10] which requires prior considerations in the manufacturing processes.

From the above discussion, it is evident that a generalized ready to use solution would be very useful in case the drone body material gets changed [19] or a cumbersome installation procedure is required. A thin, conformal antenna with a full ground plane (to reduce the body effect) would be very useful where the antenna can be attached to the drone's body on demand. In this work, a circular microstrip antenna is proposed where two modes are excited by carefully positioning of the feed point and the bandwidth is enhanced through parasitic patches on a thin substrate $(0.0128 \lambda_0)$. Dual mode results in two radiation patterns, as shown in Fig. 1, which is favorable for situations where a single radiation pattern such as for a monopole would result in coverage issues. The design and some initial results of the proposed antenna have been shown in [20]. This paper provides details of antenna design evolution as well as sensitivity analysis for key design parameters and a detailed discussion on surface currents and antenna radiation modes. Further, this paper shows the design of a 3-element MIMO configuration to ensure high data rates that can sustain a high-quality HD video transmission. Various key MIMO parameters such as envelop correlation coefficient (ECC), active reflection coefficient (ARC), directive gain (DG) and total active reflection (TARC) are studied. Additionally,
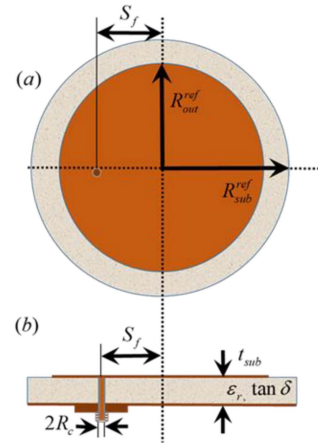
antenna characterization on various real-world scenarios, such as bending at different radii and mounting on UAV body has been performed in both numerical simulations as well as measurements. The radiation patterns for various bending radii is also included here to demonstrate antenna's insensitivity under moderate bending conditions.

A comparison of UAV antennas is given in Table 1 to show the viability of the proposed antenna. Here, we can see that the proposed antenna exhibits one of the largest bandwidths for both the bands despite being on one of the thinnest substrate. Further, it demonstrates one of the highest gain and diverse radiation patterns that will lead to large communication range and wide radiation coverage. Finally, the antenna being thin and conformal, can be seamlessly integrated with the UAV body without any deterioration in performance due to bending or UAV body effect.

II. DUAL-MODE ANTENNA DESIGN
A. REFERENCE ANTENNA DESIGN
As a first step, a conventional circular microstrip antenna is designed to act as a reference antenna, as shown in Fig. 2. The substrate radius of the reference antenna is kept as R_{sub}^{ref} while R_{out}^{ref} represents circular driven patch radius. This antenna is designed on a thin-flexible Roger 5880 substrate with dielectric permittivity of 2.2 and loss tangent of 0.0009. The antenna has a full ground plane, as shown in the side view in Fig. 2(b). It is well known that with the substrate height $t_{sub} << \lambda$, the circular patch supports TM^z modes, where z represents a directions normal to the patch. The resonant frequencies for TM_{mn0}^z modes, i.e., $(f_r)_{mn0}$ can be expressed as

$$(f_r)_{mn0} = \frac{1}{2\pi \sqrt{\mu\varepsilon}} \left(\frac{\chi'_{mn}}{R_{out}^{ref}} \right). \tag{1}$$

The permeability and permittivity of the substrate material are represented as μ, ε, whereas χ'_{mn} is a constant defining the antenna modes ($\chi'_{11} = 1.8412$, $\chi'_{21} = 3.0542$, $\chi'_{01} = 3.818$ and $\chi'_{31} = 4.2012$). An optimum feed point S_f is

TABLE 1. State-of-the-art comparison for UAV antennas with ground planes.

#Ref	Antenna type	Antenna height (λ_0) (physical height in mm)	Bandwidths MHz	Max. Gain (dBi)	Antenna Aperture (mm²)	Dual-band	Seamless Integration	Pattern Diversity
[4]	Higher-order mode circular patch	0.042 λ_0 (18 mm)	NA	5.0	1.96 λ_0^2	No	No	No
[6]	HMCPA	0.023 λ_0 (10 mm)	16 (2.2 %)	1.86	1.90 λ_0^2	No	No	No
[10]	Rectangular patch array	0.049 λ_0 (6 mm)	120 (4.8 %)	1.3	0.93 λ_0^2	No	No	No
[9]	Annular slot antenna	0.271 λ_0 (3.05 mm)	70 (2.6 %)	2.67	0.55 λ_0^2	No	No	No
[12]	Folded strip antenna	0.05 λ_0 (30 mm)	11 (2.2 %)	4.8	-	No	No	No
[16]	Cloverleaf antenna	0.232 λ_0 (28.4 mm)	100 (4.0%)	6.38	1.28 λ_0^2	No	No	No
[17]	E-shaped microstrip patch	0.0384 λ_0 (4.8 mm)	164 (6.6% @2.4 GHz) 246 (4.8%@5.8 GHz)	6.8 (2.4 GHz) 2.1 (5.2 GHz)	0.64 λ_0^2	Yes	No	No
[18]	Shorted microstrip antenna	0.0336 λ_0 (4.0 mm)	90 (3.7% @2.4 GHz) 277 (5.3% @5.2 GHz)	4.1 (2.4 GHz) 1.4 (5.2 GHz)	0.08 λ_0^2	Yes	No	No
[13]	Arc shaped slot patch antenna	0.06 λ_0 (11.57 mm)	47 (2.9% @1.575GHz) 125(5.1% @2.45 GHz)	7.07 (1.57 GHz) 7.47 (2.45 GHz)	0.64 λ_0^2	Yes	No	No
This work	Dual mode circular patch antenna with parasitic patches	0.0128 λ_0 (1.57 mm)	97 (3.9% @2.4 GHz) 360 (6.9%@ 5.2 GHz)	9.55 (2.4 GHz) 8.50 (5.2 GHz)	1.16 λ_0^2	Yes	Yes	Yes

TABLE 2. Design parameters for reference antenna (in mm).

R_{sub}^{ref}	R_{out}^{ref}	S_f	R_c	t_{sub}
30.86	23	7.41	1.2	1.57
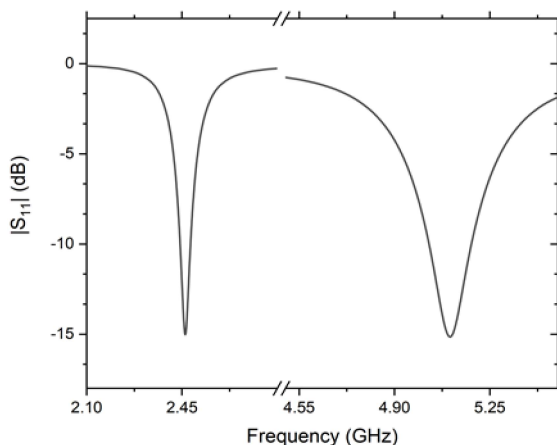
FIGURE 3. Simulated reflection coefficient of the reference circular microstrip patch antenna.
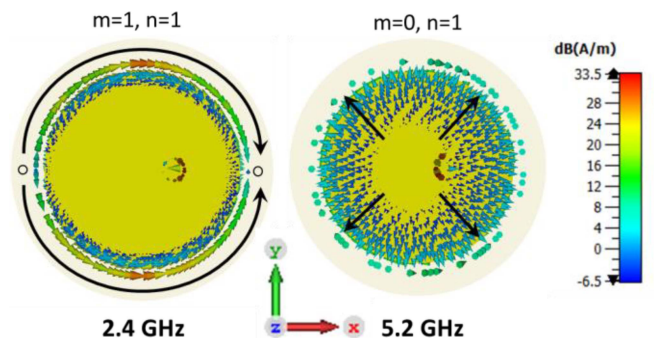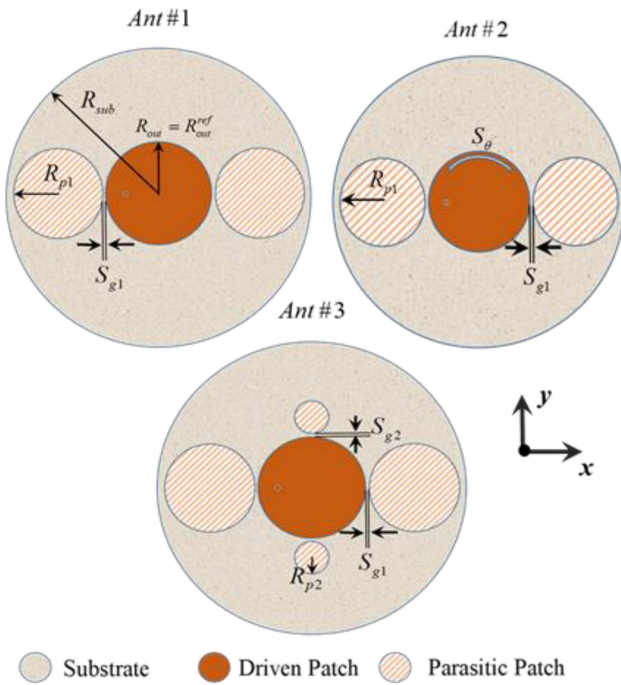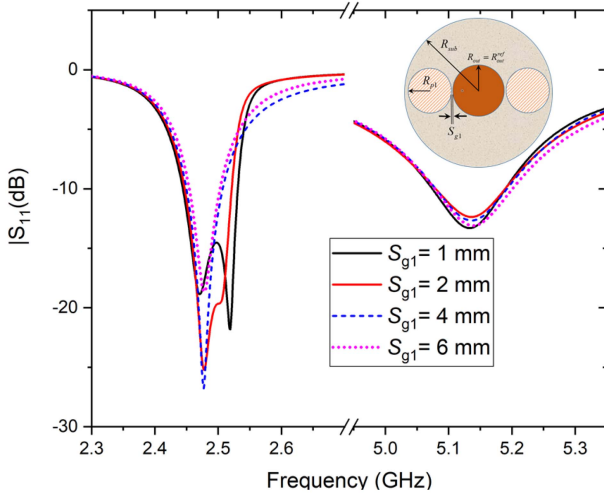
FIGURE 4. Simulated surface current distribution at 2.4 GHz and 5.2 GHz bands.

symmetrical for the *x*-axis and higher magnitude of currents are observed along the edges of positive and negative *y*-axis. On the other hand, the current are flowing from center to the outer periphery at the 5.2 GHz band. Interestingly, the magnitude of current is uniform along the periphery of the patch at the 5.2 GHz band while at 2.4 GHz current showing a wavelength variation along the periphery.

B. DESIGN EVOLUTION: BANDWIDTH ENHANCEMENT

The BW enhancement of reference antenna is considered here through multiple ways such as parasitic patches, slots or by combining both the techniques. Three antenna configurations, labeled as Ant #1, Ant #2, and Ant #3, as shown in Fig. 5, are investigated. To accommodate the parasitic patches, the substrate radius is increased for all three configurations and termed here as R_{sub}. The first configuration shown, i.e., Ant #1, is mainly using two identical parasitic patches placed along the *x*-axis. The radius of the parasitic patches is termed as R_{p1} while the radius of the driven patch is kept the same as that of the reference antenna, i.e., R_{out}^{ref}. The edge-to-edge gap between the driven patch and the parasitic patches is S_{g1}. The second configuration, i.e., Ant #2 introduces an additional radial slot of angle S_{θ} in the driven patch. The third and final configuration uses

chosen such that the antenna resonates at two modes, i.e., TM_{11} and TM_{01} simultaneously. Two modes, i.e., TM_{11} and TM_{01} are selected to get the appropriate frequency ratio for covering the both ISM bands, i.e., 2.4 GHz and 5.2 GHz as

$$\frac{(f_r)_{TM_{01}}}{(f_r)_{TM_{11}}} = \left(\frac{\chi_{01}'}{\chi_{11}'}\right) = 2.081. \qquad (2)$$

Antenna dimensions listed in Table 2 are used as the model parameters and simulations are conducted in the commercial 3D electromagnetic simulator. The antenna is fed by a wave port representing a coaxial feed. Fig. 3 shows the simulated reflection coefficient of the reference antenna. It is found here that the simulated −10 dB bandwidths (BW) at 2.4 GHz and 5.2 GHz bands are 38 MHz and 155 MHz respectively. Fig. 4 shows the simulated current density distribution of the two resonant modes, i.e., 2.4 GHz (TM_{11}) and 5.2 GHz (TM_{01}) bands. For TM_{11} mode, the current distribution is

FIGURE 5. Different antenna configurations for the bandwidth enhancement.

FIGURE 6. *Ant # 1:* Reflection coefficient for varying gap S_{g1} while keeping $R_{p1} = 22.50$ mm.

FIGURE 7. *Ant # 1:* Reflection coefficient for varying R_{p1} while keeping $S_{g1} = 1.0$ mm.

FIGURE 8. *Ant # 2:* Reflection coefficient for varying S_{θ} while keeping $S_{g1} = 1.0$ mm.

TABLE 3. Optimized antenna design parameters (in millimeters).

$R_{sub}^{Ant2} = R_{sub}^{Ant3}$	R_{out}^{ref}	R_{p1}	R_{p2}	S_{g1}	S_{g2}
76	23.25	22.90	10.19	0.98	0.15

additional identical parasitic patches along the *y*-axis of the radius with an edge-to-edge gap with the driven patch of S_{g2}.

For instance, the first antenna configuration also termed here as Ant #1, parasitic patches for the enhancement of BW at 2.4 GHz are introduced. As presented in [21], the parasitic patches can be positioned in the vicinity of the driven patch and gets excited by the radiating edges as well as from the non-radiating edges. To see the effect of parasitic patches on the resonance of the driven reference patch, a relatively smaller parasitic patch compared to the driven patch is chosen. In Fig. 6, the reflection coefficient for different gaps, i.e., S_{g1} between the driven and parasitic patches is
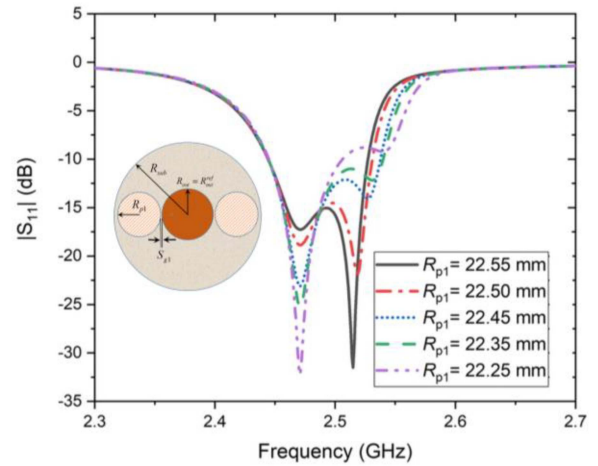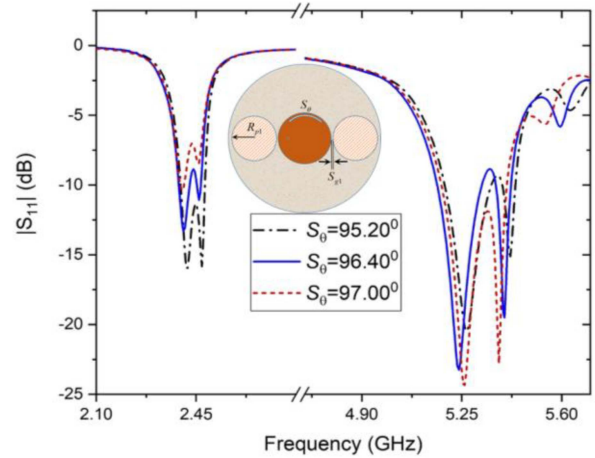
shown. It is observed that when the parasitic patches come closer to the driven patch $S_{g1} < 2$ mm, a second resonance appears within the 2.4 GHz band. This second resonance is due to the proximity coupling between the driven and the parasitic patches (due to the fringing fields). It is also observed that the impedance BW of the antenna is enhanced by the introduction of the parasitic patches, while there is negligible effect on the other frequency band, i.e., 5.2 GHz band. The radius of parasitic patches is usually chosen to create an additional resonance as seen in Fig. 6 and gap between them could provide sufficient coupling for exciting parasitic patches.

In Fig. 7, the effect of varying parasitic patches radii with a fixed edge-to-edge gap is shown. It can be seen here that the resonance due to the introduction of parasitic patches can
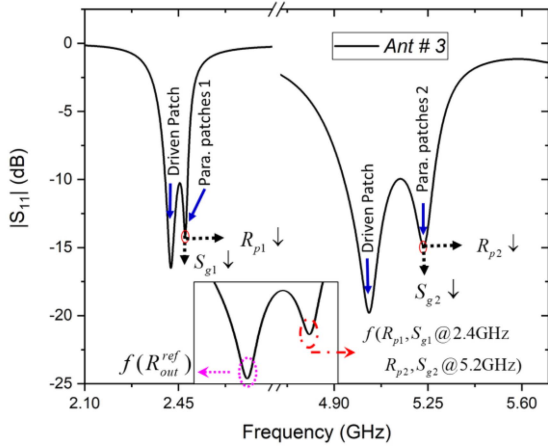
FIGURE 9. *Ant # 3:* Reflection coefficient of the proposed antenna with optimized dimension as mentioned in Table 3.
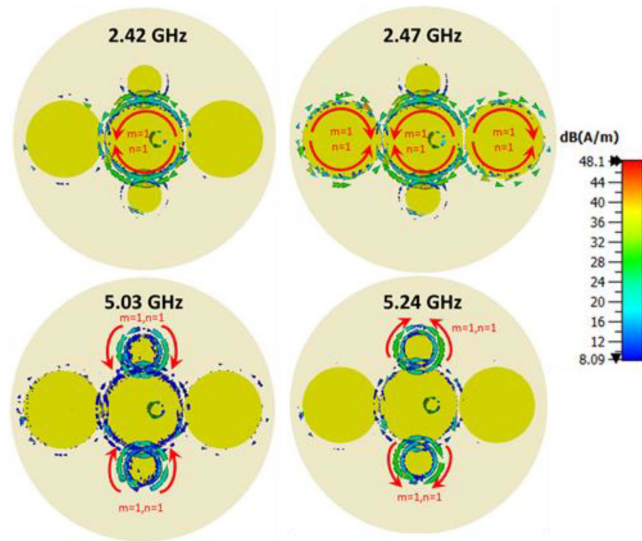

FIGURE 10. Surface current distribution over the proposed antenna for four resonant frequencies.

FIGURE 11. *Ant # 3:* Proposed antenna radiation and return loss characteristics (a) 2.4 GHz band, and (b) 5.2 GHz band, while mounted conformally on a drone wing (made up of PEC).

be tuned towards or away from the driven patch resonance by varying the radii of the parasitic patches. This parametric variation can be optimized to enhance the antenna bandwidth significantly. As mentioned earlier, Ant #1 configuration, enhances the BW at the 2.4 GHz band without affecting the matching performance at the second band (i.e., 5.2 GHz band). For increasing the bandwidth at the 5.2 GHz band, a radial slot of angle S_θ is introduced along the periphery of the driven patch. The slot of 1.5 mm width is made at a spacing of 1.2 mm from the outer edge of the driven patch as shown in Fig. 5. It can be seen that the slot introduces an additional resonance at the 5.2 GHz band, however, it disturbs the antenna matching performance at the 2.4 GHz band when the radial angle is > 95°. This slot is resonating on a higher order dipole mode and is not under the influence of adjacent mode, i.e., TM_{02}. One can still enhance the antenna bandwidth at both bands as shown in Fig. 8 as long as the additional slot does not affect the coupling between
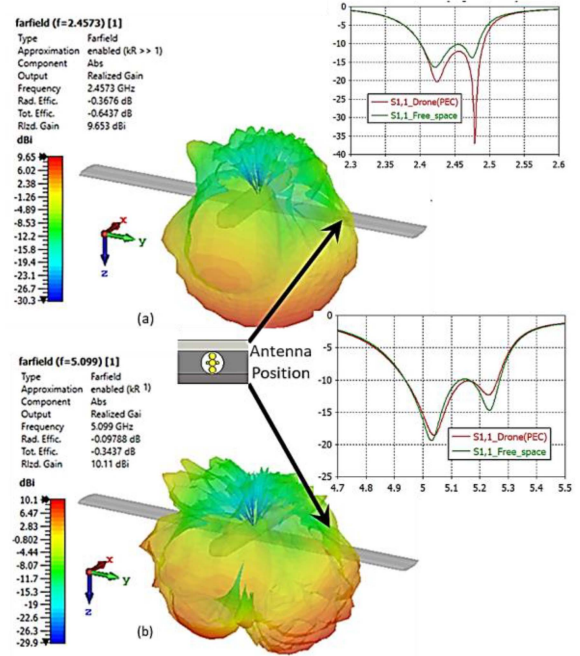
the driven and parasitic patches at 2.4 GHz. We have found that for Ant #2, the maximum BW at 2.4 GHz is 93 MHz (reference antenna has 38 MHz) while at 5.2 GHz, the BW is 235 MHz (reference antenna has 155 MHz). It is well known that the principle of operation of such slots is to alter the distribution of current to achieve the required performance enhancement in the antenna. However, in the present scenario, if the current distribution is changed significantly due to the introduction of the slot, the performance for the other band, i.e., 2.4 GHz is degraded. This is quite obvious as the parasitic patches have been introduced with respect to the current distribution at 2.4 GHz. To keep the first band (i.e., 2.4 GHz) insensitive while enhancing bandwidth at the second band (i.e., 5.2 GHz), we need to devise a mechanism by which the current distribution of the driven patch does not get affected significantly. We introduced another pair of the parasitic patches with radius R_{p2} on along the y-axis at a relatively low edge-to-edge gap S_{g2} in our final antenna design (i.e., Ant # 3). The reason for keeping a relatively low edge-to-edge gap S_{g2} can be explained by the low-intensity surface currents at the 5.2 GHz band as compared to the 2.4 GHz band (Fig. 4). A smaller edge-to-edge gap provides sufficient coupling to the added parasitic patches for the 5.2 GHz band. Later, an optimization routine (particle swarm optimization) of key parameters, i.e., R_{out}^{ref}, R_{p1}, R_{p2}, S_{g1} and S_{g2} is carried out for the best impedance BW performance at both the bands, and the optimized antenna parameters are listed in Table 3. Fig. 9 shows the reflection coefficient for the proposed antenna along with the parametric sensitivity for the key design parameters. The proposed antenna exhibits
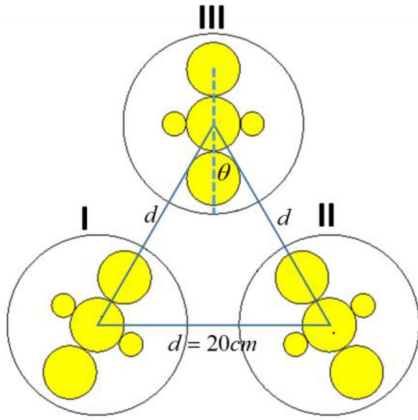
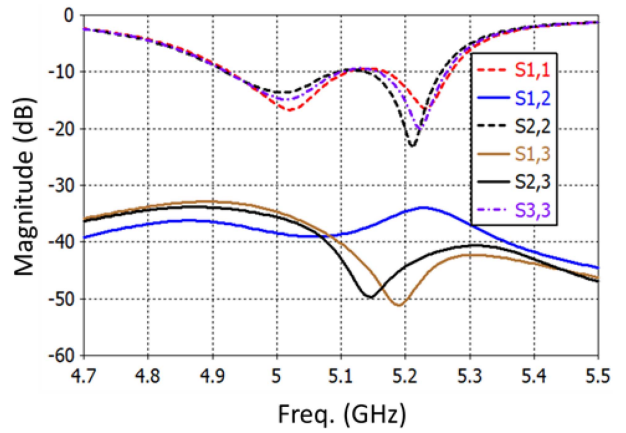**FIGURE 12.** 3-element triangular MIMO antenna configuration.

FIGURE 14. Scattering parameters at 5.2 GHz band for proposed 3-element MIMO configuration.
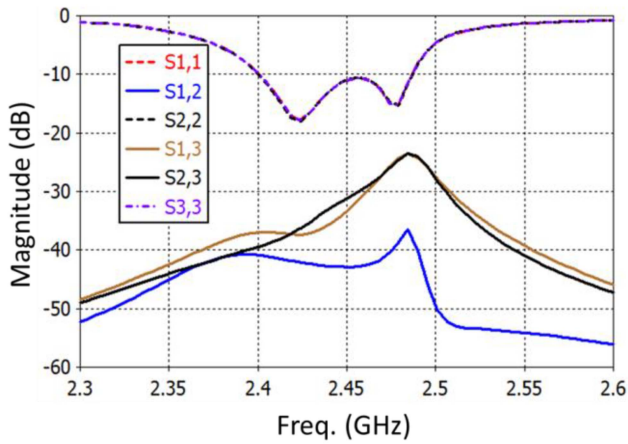

FIGURE 13. Scattering parameters at 2.4 GHz band for proposed 3-element MIMO configuration.
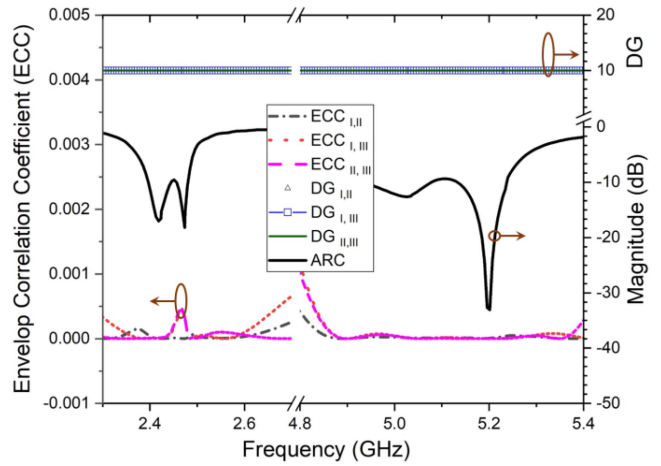

FIGURE 15. MIMO parameters for configuration shown in Fig. 12.

a fair amount of BW enhancement for both the bands and achieved BW at 2.4 GHz band is 97 MHz while at 5.2 GHz is 360 MHz.

Fig. 10 shows the surface current distribution on the proposed antenna for all four resonance frequencies, i.e., 2.42 GHz, 2.47 GHz, 5.03 GHz and 5.24 GHz. At 2.42 GHz, driven patch is exited with TM_{11} and at 2.47 GHz, the parasitic patches also gets excited with TM_{11}. As shown Fig. 4, the driven patch gets excited with TM_{01} mode at 5.2 GHz band, the electromagnetic coupling due to fringing fields exciting the parasitic patches at 5.03 GHz and 5.24 GHz respectively. By observing the current distribution at 5.03 GHz, the driven and parasitic patches effectively contributes towards the radiation. However, at 5.25 GHz, significant current is flowing along the edges of parasitic patches as compared to driven patch confirms radiation elements.

To further clarify the utility of the proposed antenna for plug-and-play installation on a drone, as well as for wider coverage (Fig. 1: case-1 and case-2), another simulation is performed while the antenna is conformally mounted on a drone wing made of PEC and its radiation pattern for both
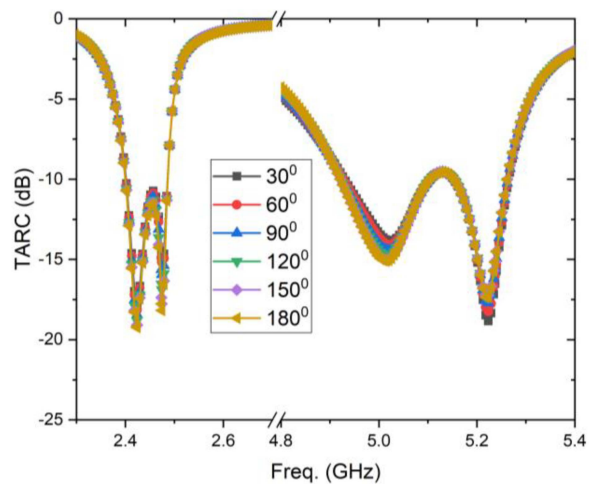

FIGURE 16. Total active reflection coefficient (TARC) of the proposed MIMO configuration.

the bands is shown in Fig. 11. The antenna's impedance BW and radiation patterns are not affected much when integrated with the drone surfaces.
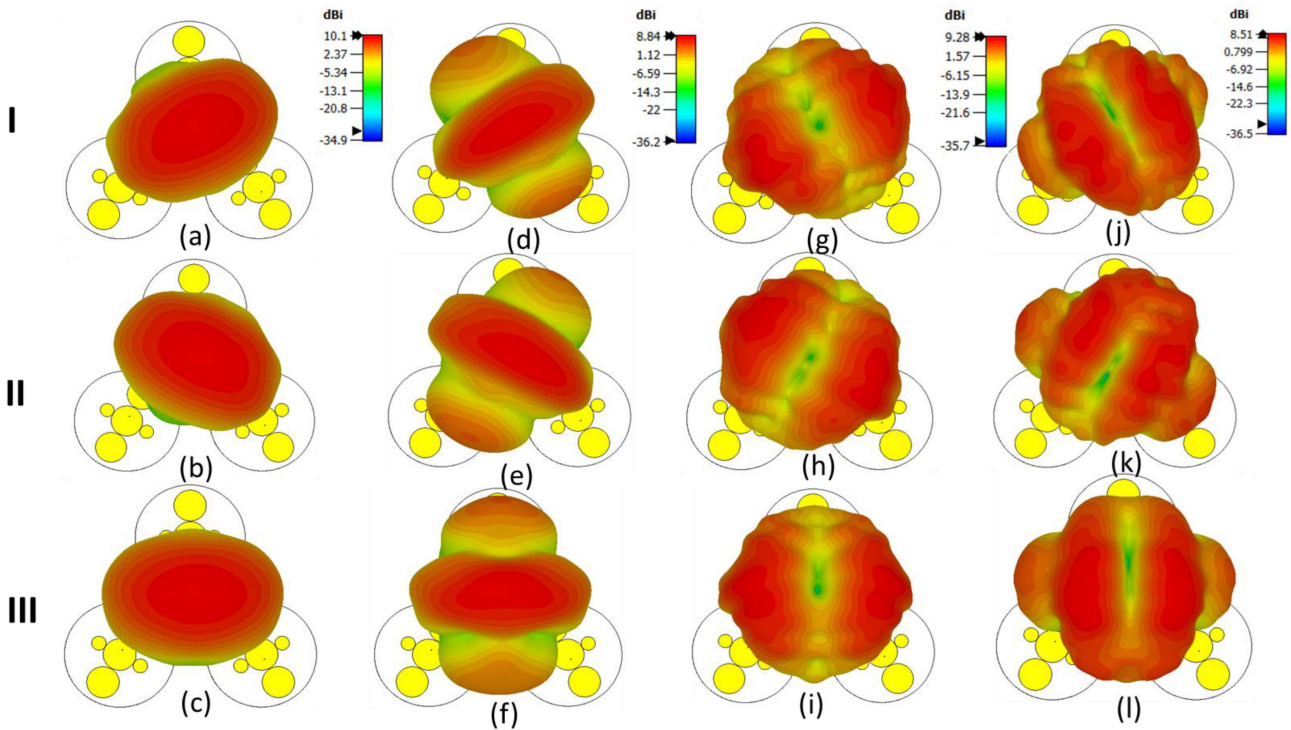
FIGURE 17. Radiation pattern of individual antenna in MIMO configuration (a), (b), (c) at 2.42 GHz for driven patches (d), (e), (f) at 2.47 GHz for parasitic patch (g), (h), (i) 5.03 GHz for driven patches and (j), (k), (l) 5.24 GHz for parasitic patches.

III. PROPOSED MIMO CONFIGURATION

A 3-element MIMO configuration, employing the proposed antenna in a triangular orientation, is shown in Fig. 12. The antenna elements are arranged on the vertices of an equilateral triangle with a side dimension of $d = 200$ mm. The antenna I and II are rotated by $\theta = 30^0$ clockwise and counter-clockwise respectively with respect to III. This MIMO configuration is simulated and reflection coefficients of each antenna element and mutual coupling between them are plotted in Figs. 13 and 14 for 2.4 GHz and 5.2 GHz bands respectively. The reflection coefficient of each antenna element shows a consistent -10 dB bandwidth and fairly good isolations, i.e., > 20 dB between the antenna elements for both the bands. As explained earlier, the first resonance belongs to the driven patch whereas the second resonance is due to the parasitic patches. It can be seen in Fig. 13, the mutual coupling between antennas I and II is much lower when compared to the coupling between antennas I and III or antennas II and III, because of larger separation between radiating elements of I and II. In a similar manner the higher mutual coupling between the antennas I and II in Fig. 14 can be explained for the 5.2 GHz band. It is worth mentioning here that the isolation is > 35 dB for the range of frequencies where the driven patch is dominant.

Various MIMO parameters such as ECC, DG and TARC are calculated with the procedure given in [22] and plotted for both the frequency bands in Figs. 15 and 16. From Fig. 15, it is evident that the ECC is well below 0.005 which confirms legitimately good isolation between
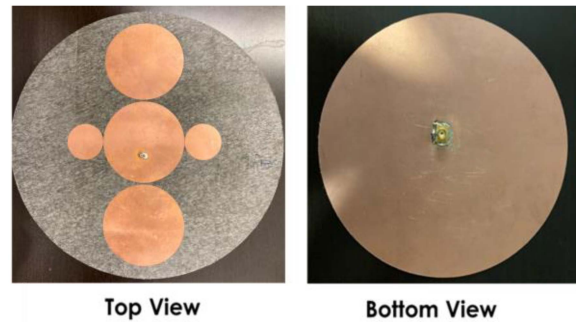

FIGURE 18. Fabricated prototype antenna.

the antenna elements. As the correlation coefficient is well below 0.005, the DG values are consistently around 10. It is to be noted here that the ECC and DG are calculated from *S*-parameters. The TARC response for different phases shown in Fig. 16 indicates a decent MIMO configuration as it covers almost the similar -10dB bandwidths as of individual antenna without any significant deviation. Fig. 17 shows the radiation patterns of the individual antenna in the MIMO array. Fig. 17(a)-(c) and (g)-(i) are showing the radiation characteristics at resonance frequencies (i.e., 2.42 GHz and 5.03 GHz) when the driven patch is dominant, whereas Fig. 17(d)-(f) and (j)-(l) are showing the radiation patterns at 2.47 GHz and 5.24 GHz when the parasitic patches also get excited. The radiation patterns for the parasitic patches add grating lobes in addition to the major radiation lobes
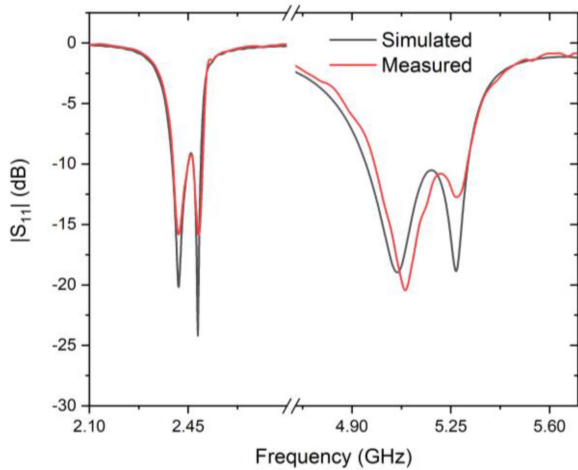
FIGURE 19. Comparison of measured and simulated reflection coefficient for the proposed antenna.
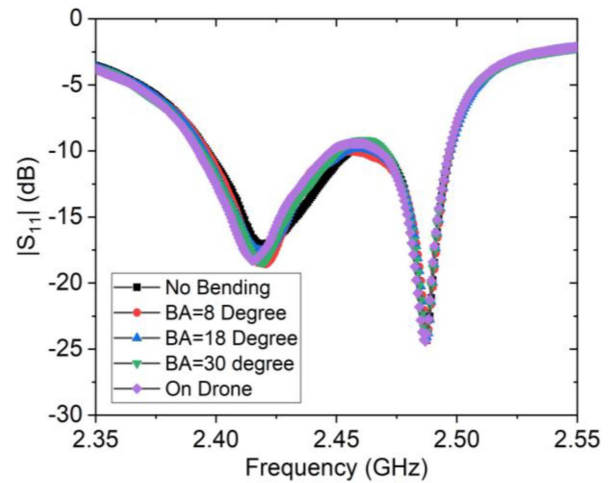

(a)

(b)

FIGURE 20. (a) Antenna measurement on bending condition, and (b) seamless integration of the antennas on UAV wings.

(a)

(b)

FIGURE 21. Antenna reflection coefficient (a) 2.4 GHz band, and (b) 5.2 GHz band for various bending angles and UAV mounted antenna.

then connected such that its center pin connects with the top driven-patch and the ground base with the antenna's ground plane. The reflection coefficient of the fabricated antenna is then measured in a laboratory environment employing the vector network analyzer (PNA Keysight E8363C). The measured and simulated reflection coefficients are plotted as shown in Fig. 19 for both 2.4 and 5.2 GHz bands. A fair agreement between simulated and measured results can be observed and a slight deviation at the 5.2 GHz band that is due to the fabrication inaccuracy of the gap dimension, i.e., S_{g2}.

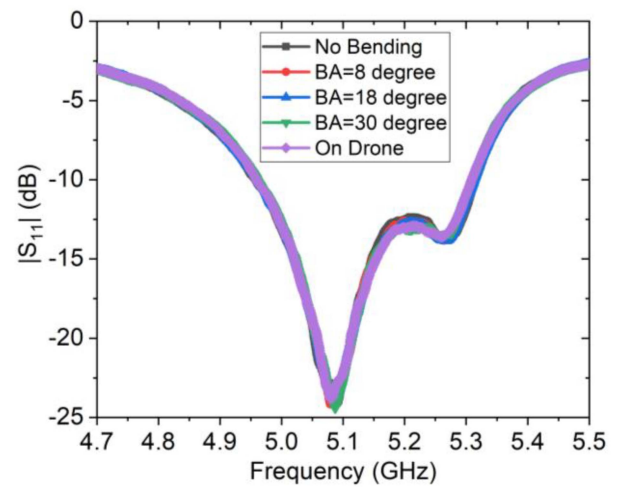that help in radiation coverage for the lower altitude of the elevation plane.

IV. RESULTS AND DISCUSSION
A. FABRICATION AND REFLECTION COEFFICIENT CHARACTERIZATION
The proposed antenna is fabricated on semi-flexible substrate (Rogers© 5880, $\varepsilon_r = 2.2$ and, $\tan\delta = 0.0009$) as shown in Fig. 18. The laser prototyping machines LPKF Protomat U3 and Protomat H100 are used for etching the structure and making a plated through vias for feeding. The SMA jack is

B. ANTENNA BENDING PERFORMANCE
To see the antenna performance in different bending conditions, the antenna is bent in 3 bending angles viz. 8, 18 and 30 degrees as depicted in Fig. 20(a) to accommodate a typical curvature of UAV's body. Our antennas can be mounted on wings or fuselage of UAV. To show actual seamless integration, our antennas are mounted on
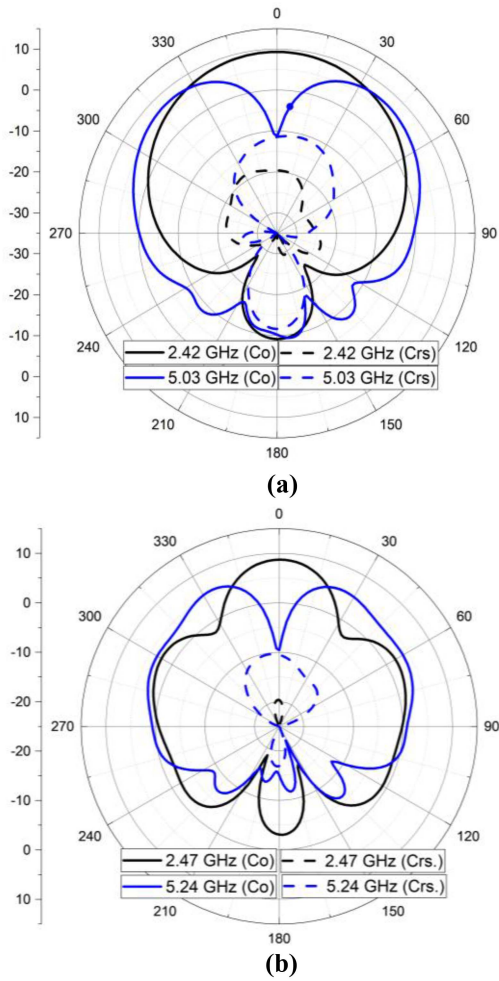
FIGURE 22. Measured antenna radiation pattern for both the frequency bands (a) at driven patch resonance frequencies {$\phi = 90°$ for 2.42 & 5.03 GHz} and (b) at parasitic patch resonance frequencies {$\phi = 0°$ @ 2.47 GHz and $\phi = 90°$ @ 5.24 GHz}.

FIGURE 23. Measured antenna radiation pattern for various bending angles (a) 2.42 GHz {$\phi = 90°$} (b) 2.47 GHz {$\phi = 0°$} (c) 5.09 GHz {$\phi = 90°$} and (d) 5.25 GHz {$\phi = 90°$}.

the wings and fuselage of a drone as shown in Fig. 20(b). The considered bending scenarios are emulating the usability of the proposed antenna for typical mounting conditions. The reflection coefficients is measured for the considered bending scenarios as well as when the antenna is mounted on the UAV wing (shown in Fig. 21 along with the no bending case). Based on the observed performance for the considered bending angles, it can be established that the impedance BW of the antenna does not change much as compared to the flat antenna in air. This confirms that the antennas can be mounted easily on drones with different body material without optimizing the antenna. Also, since they are very thin and mechanically flexible they can be seamlessly integrate with the UAV body and it is expected that this integration will not affect the UAV aerodynamics.

C. 2D RADIATION PATTERN

The antenna's radiation performance characterization for both the bands is performed in an anechoic environment as shown in Fig. 20(a). The 2D radiation patterns for the
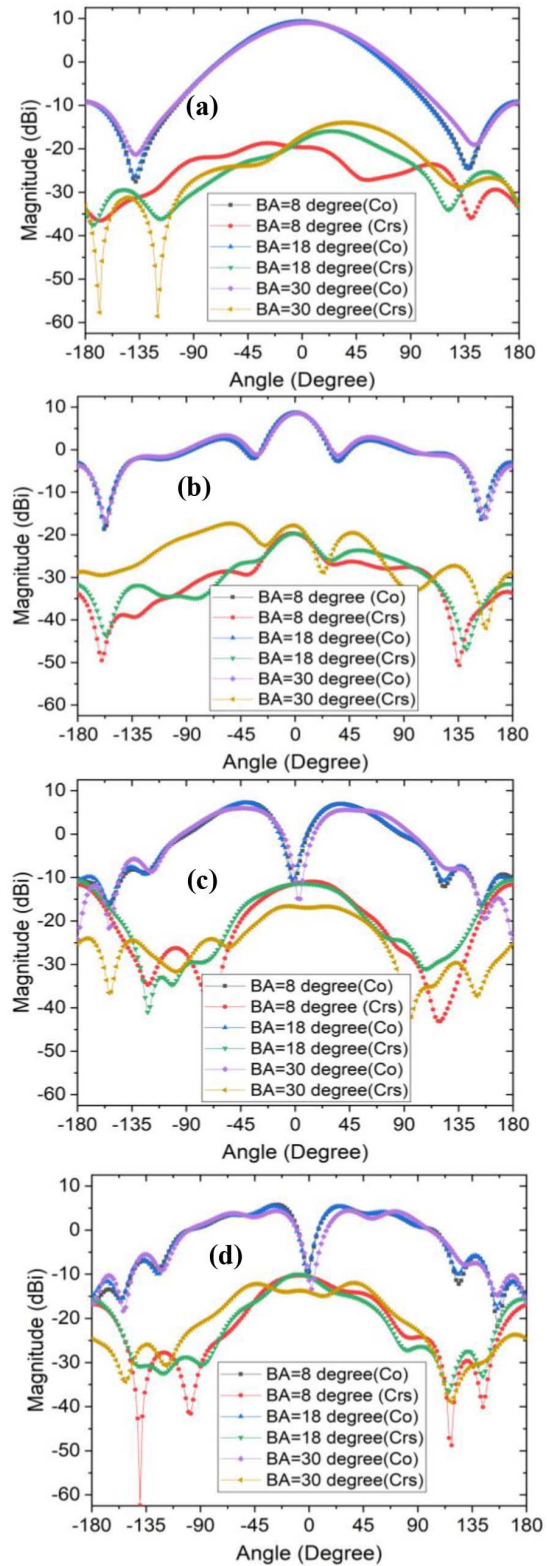
proposed antenna are plotted in Fig. 22(a) and 22(b) at the respective resonance frequencies corresponding to the driven and parasitic patches. For the resonance frequencies

corresponding to parasitic patches, two grating lobes appears in the radiation patterns for both the bands. Though, grating lobes decreases the overall gain of the antenna, but they are helpful in improving radiation coverage for the lower elevation angles. It can be seen from Fig. 22 that the proposed antennas radiate in the broadside direction with a peak gain of 9.55 dBi at 2.42 GHz and 6.82 dBi at 2.47 GHz. For the higher band, antenna radiates in a quasi-omnidirectional mode with a peak gain of 8.5 dBi at 5.03 GHz and 7.35 dBi at 5.24 GHz. To see the antenna radiation pattern under various bending condition as depicted in Fig. 20(a), the radiation pattern measurement is performed for various bending angles viz. 8°, 18° and 30° for all 4 resonance frequencies and plotted in the Fig. 23(a)-(d). For all frequencies, the co-polarized component shows pretty consistent performance against bending's and cross-polar component is well below (between −20 dB to −30 dB) from the radiation spheres.

V. CONCLUSION

A circular microstrip antenna is designed, fabricated and characterized that resonates at two modes simultaneously with a single feed location. Various bandwidth enhancement techniques viz. slot and parasitic elements are investigated to increase the impedance bandwidth of the antenna. The proposed antenna, which has the highest gain and the BW amongst all published UAV antennas, is designed, such that the individual band performance can be tuned independently without affecting the other band significantly. The performance comparison indicates a fair agreement between the measured and simulated results. The antennas performance has been assessed for various bending and mounting situations to show its usability for a typical UAV mounting conditions. A closely spaced 3-element MIMO configuration has been analyzed and various key parameters are calculated. Thin and flexible nature of the proposed antenna makes it attractive for a seamless integration with the UAVs surface. The proposed MIMO configuration can be used to achieve higher data rates for HD video transmission to larger distances as compared to the conventional antennas such as monopoles and annular slot antennas with relatively low gains. Furthermore, the full ground plane also reduces the body effect that makes this design appealing for a generalized plug-and-play solution irrespective or insensitive to UAV body materials, i.e., dielectric or metal.

REFERENCES

[1] (Mar. 2020). *Drone Market-Growth, Trends, and Forecast.* [Online]. Available: https://www.reportlinker.com/p05881491/Drones-Market-Growth-Trends-and-Forecast.html?utm_source=GNW

[2] M. Nosrati, A. Jafargholi, R. Pazoki, and N. Tavassolian, "Broadband slotted blade dipole antenna for airborne UAV applications," *IEEE Trans. Antennas Propag.*, vol. 66, no. 8, pp. 3857–3864, Aug. 2018.

[3] D. M. Moorehouse and A. Humen, *Improved UAV Datalink Performance Using Embedded Antennas*, Nurad Technol., Baltimore, MD, USA, 2012, pp. 1–12.

[4] S. Yoon, J. Tak, J. Choi, and Y.-M. Park, "Conformal monopolar antenna for UAV applications," in *Proc. IEEE Int. Symp. Antennas Propag. USNC/URSI Nat. Radio Sci. Meeting*, San Diego, CA, USA, 2017, pp. 517–518.

[5] Z.-Q. Liu, Y.-S. Zhang, Z. Qian, Z. P. Han, and W. Ni, "A novel broad beamwidth conformal antenna on unmanned aerial vehicle," *IEEE Antennas Wireless Propag. Lett.*, vol. 11, pp. 196–199, 2012.

[6] J. Tak and J. Choi, "A flush-mounted monopolar patch antenna for UAV applications," *Microw. Opt. Technol. Lett.*, vol. 59, no. 5, pp. 1202–1207, 2017.

[7] M. S. Sharawi, D. N. Aloi, and O. A. Rawashdeh, "Design and implementation of embedded printed antenna arrays in small UAV wing structures," *IEEE Trans. Antennas Propag.*, vol. 58, no. 8, pp. 2531–2538, Aug. 2010.

[8] L. I. Balderas, A. Reyna, M. A. Panduro, C. Del Rio, and A. R. Guti érrez, "Low-profile conformal UWB antenna for UAV applications," *IEEE Access*, vol. 7, pp. 127486–127494, 2019.

[9] L. Sun, B.-H. Sun, Q. Sun, and W. Huang, "Miniaturized annular ring slot antenna for small/mini UAV applications," *Progr. Electromagn. Res.*, vol. 54, pp. 1–7, Oct. 2014.

[10] D. V. Navarro-Méndez, H. C. Moy-Li, L. F. Carrrera-Suárez, M. Ferrando-Bataller, and M. Baquero-Escudero, "Antenna arrays for unmanned aerial vehicle," in *Proc. 9th Eur. Conf. Antennas Propag. (EuCAP)*, Lisbon, Portugal, 2015, pp. 1–5.

[11] M. S. Sharawi, M. Ibrahim, S. Deif, and D. N. Aloi, "A planar printed antenna array embedded in the wing structure of a UAV for communication link enhancement," *Progr. Electromagn. Res.*, vol. 138, pp. 697–715, Apr. 2013.

[12] B.-H. Sun, Y.-F. Wei, S.-G. Zhou, and Q.-Z. Liu, "Low-profile and horizontally-polarised antenna for UAV applications," *Electron. Lett.*, vol. 45, no. 22, pp. 1106–1107, 2009.

[13] J. Chen, J. Wang, K.-F. Tong, and A. Al-Armaghany, "A GPS/Wi-Fi dual-band arc-shaped slot patch antenna for UAV application," in *Proc. Loughborough Antennas Propag. Conf. (LAPC)*, Loughborough, U.K., 2013, pp. 490–493.

[14] H. F. Abutarboush, M. F. Farooqui, and A. Shamim, "Inkjet-printed wideband antenna on resin-coated paper substrate for curved wireless devices," *IEEE Antennas Wireless Propag. Lett.*, vol. 15, pp. 20–23, 2015.

[15] H. F. Abutarboush and A. Shamim, "Paper-based inkjet-printed tri-band U-slot monopole antenna for wireless applications," *IEEE Antennas Wireless Propag. Lett.*, vol. 11, pp. 1234–1237, 2012.

[16] M. Safaron *et al.*, "Directional cloverleaf antenna for unmanned aerial vehicle (UAV) application," *Indonesian J. Elect. Eng. Comput. Sci.*, vol. 14, no. 2, pp. 773–779, 2019.

[17] A. G. Ambekar and A. A. Deshmukh, "E-shape microstrip antenna for dual frequency WLAN application," *Progr. Electromagn. Res. C*, vol. 104, pp. 13–24, Jul. 2020.

[18] H.-C. Tung and K.-L. Wong, "A shorted microstrip antenna for 2.4/5.2 GHz dual-band operation," *Microw. Opt. Technol. Lett.*, vol. 30, no. 6, pp. 401–402, 2001.

[19] M. M. ElFaham, A. M. Mostafa, and G. Nasr, "Unmanned aerial vehicle (UAV) manufacturing materials: Synthesis, spectroscopic characterization and dynamic mechanical analysis (DMA)," *J. Mol. Struct.*, vol. 1201, Feb. 2020, Art. no. 127211.

[20] Z. Akhter, R. M. Bilal, and A. Shamim, "Dual-mode circular microstrip patch antenna for airborne applications," in *Proc. 15th Eur. Conf. Antennas Propag. (EuCAP)*, Dusseldorf, The Germany, 2021, pp. 1–5.

[21] G. Kumar and K. P. Ray, *Broadband Microstrip Antennas*. Boston, MA, USA: Artech House, 2003.

[22] M. S. Sharawi, *Printed MIMO Antenna Engineering*. Boston, MA, USA: Artech House, 2014.